ACS MATERIALS LETTERS

www.acsmaterialsletters.org

LETTER

Increasing the Energy Density of Disordered Rock Salt Anodes for Fast-Charging Lithium-Ion Batteries

Haichen Lin, Wei-Tao Peng, Zishen Wang, Jan Hofmann, Simon M. Vornholt, Haodong Liu, Shen Wang, John Holoubek, Ke Zhou, Qiushi Miao, Steven Huber, Karena W. Chapman,* Shyue Ping Ong,* and Ping Liu*

Cite This: *ACS Materials Lett.* 2025, 7, 699–706

Read Online

ACCESS | Metrics & More | Article Recommendations | Supporting Information

ABSTRACT: Transition-metal oxides (TMOs) are promising anode materials for safe and fast-charging batteries, but their high operating potentials limit energy density. Here, we develop a strategy to suppress the operating potential of the disordered rock salt (DRS) $Li_3V_2O_5$ (LVO) anode by ∼10% to 0.54 V via Mg doping. Density functional theory (DFT) calculations attribute this voltage reduction to increased site energy of Li ions because of Mg doping, with minimal impact on Li migration barriers. Mg-doped LVO retains over 95% of its capacity over 1000 cycles at a rate of 5 C. Full cells with a $LiNi_{0.8}Co_{0.1}Mn_{0.1}O_2$ cathode demonstrate the expected increase in cell voltage and energy density while retaining 91% of their capacity over 250 cycles at 5 C. Our findings show that Mg doping provides a promising pathway for designing fast-charging, long-cycle-life anode materials with enhanced energy density.

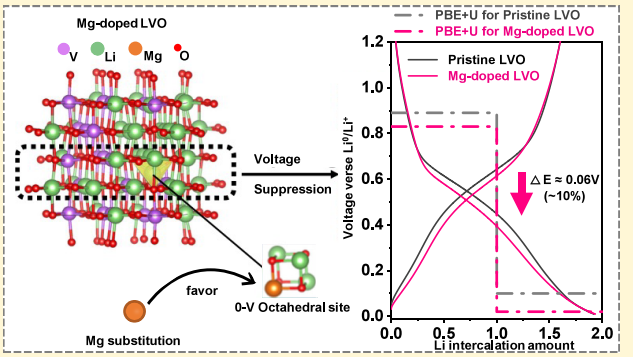

Lithium-ion batteries remain the energy storage of choice for both vehicle and grid applications, although significant progress has been made with next-generation batteries.[1−3] Recent analysis shows that batteries with energy densities suitable for vehicle propulsion and a long life (>5000 cycles and 30 years) would be transformational for the grid.[4] Such batteries promise to enable ubiquitous vehicle to grid (V2G) integration when coupled with the fast-charging capabilities. This would significantly reduce the overall demand for battery material and manufacturing capacity.[4−6]

In Li-ion batteries, the graphite anode dictates their fast charging and cycle life capabilities. Graphite experiences a 10% change in spacing between the graphene sheets during charge and discharge, which can lead to breaking of the solid electrolyte interface (SEI) layer[7] and capacity loss.[8] Transition-metal oxides (TMOs), for example, $Li_4Ti_5O_{12}$ (LTO), Li_3VO_4, and $TiNb_2O_7$ (TNO), have been considered as alternatives due to their minimal volume changes during cycling. However, their working potentials of over 1 V vs Li lead to a reduction in cell voltage and energy density.[9−11] Therefore, it is crucial to develop oxide materials that operate at a lower potential.

Recently, we have introduced a disordered rock salt (DRS) anode, DRS-$Li_3V_2O_5$ (LVO).[12] This material can be cycled reversibly with ∼2 Li intercalating/extracting at an average potential of 0.6 V, significantly lower than other oxides. Its minimal, isotropic volume change during cycling (5.9%) translates to an exceptionally long cycle life. The work motived follow-on efforts, including improving the low-temperature rate capability by using a chemically synthesized LVO material with an ether-based electrolyte.[13] The use of fluorine-containing additives led to further improvement in stability by promoting the formation of LiF-rich interphases.[14] To improve the LVO material itself, a stepwise preintercalation of polyaniline and Na ions was shown to facilitate access to charge storage sites.[15]

One approach to further improve LVO is to lower the operating potential, which will directly translate into higher full-cell voltage and energy density. Inspired by elemental doping research in layered cathode materials,[16,17] this study examines the effects of magnesium (Mg) doping on the DRS anode material, LVO. The ionic radius of Mg^{2+} (0.72 Å) is very

Received: October 12, 2024
Revised: January 16, 2025
Accepted: January 17, 2025

https://doi.org/10.1021/acsmaterialslett.4c02086
ACS Materials Lett. 2025, 7, 699−706

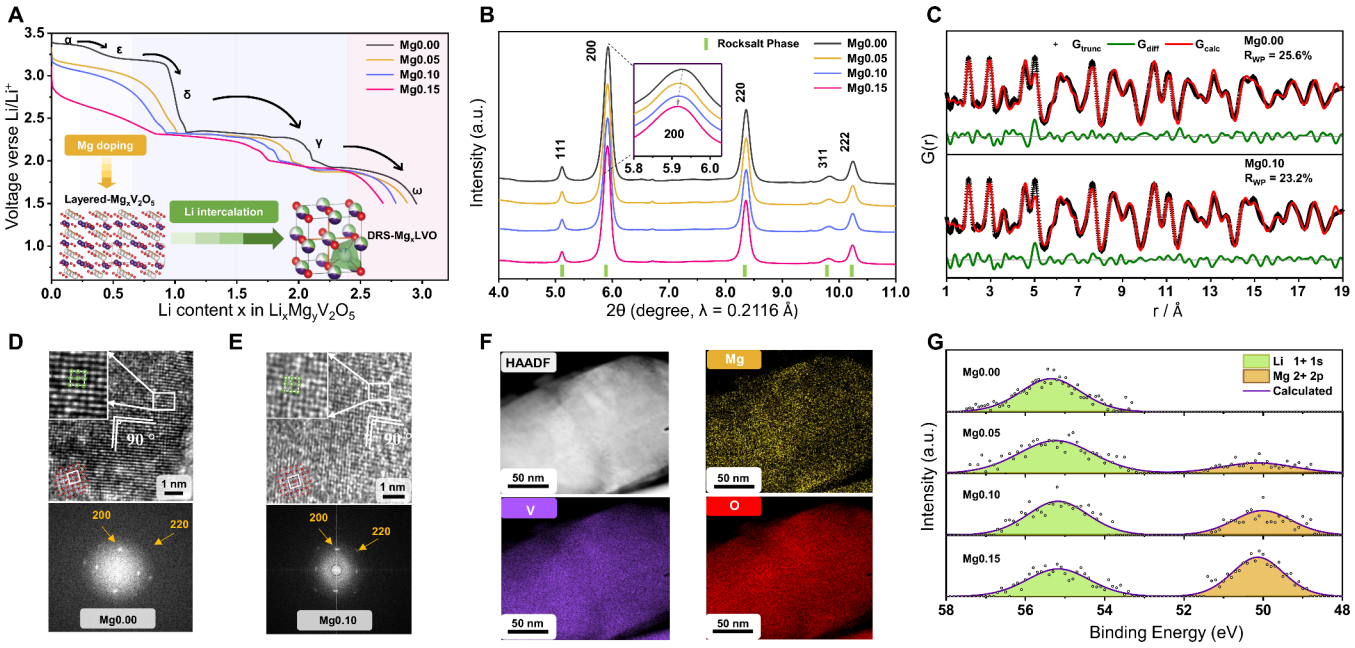

Figure 1. Synthesis and characterizations of Mg-doped LVO. (A) In-situ synthesis of Mg-doped LVO via electrochemical lithiation. (B) SXRD patterns for all materials. (C) PDF analysis for Mg0.00 and Mg0.10. (D, E) HRTEM images and FFT analysis of Mg0.00, Mg0.10. (F) Elemental mapping of Mg0.10. (G) XPS spectra and fitting results of Li 1s and Mg 2p.

close to that of Li^+ (0.76 Å),[18,19] making it an ideal candidate for doping into the DRS LVO structure.[18−21] In layered TMO oxides, Mg^{2+} has been reported to be quasi-immobile inside the lattice,[22] stabilizing the structure[18] due to its strong Coulombic interactions with anions and providing minimal hindrance to Li migration.[23,24] Fantai et al. studied the effect of doping on the voltage of $LiMnO_2$ and Li_2MnO_3.[20] Among 10 elements, they identified Mg with the greatest likelihood of occupying the Li site thus reducing lithium extraction potential. Sallard et al. further examined this effect by doping $LiNi_{0.8}Co_{0.1}Mn_{0.1}O_2$ (NCM) with different Mg ratios,[23] while Loraine et al. investigated Li_2MnO_3, confirming the decrease in redox potential with Mg doping.[25] This voltage suppression effect is also observed in the DRS TMO cathode system.[26]

Unlike cathodes, a reduction in operating potential is desirable for anodes. Through a combination of theoretical calculations and experimental validation, our study reveals that Mg doping successfully suppresses the LVO anode's potential without compromising its rate capability and cycle life. This finding provides a new direction for designing fast-charging, long-cycle-life anode materials.

Mg-doped LVO with a DRS structure is synthesized in two steps. In the first step, chemical doping of Mg into V_2O_5 using Grignard reagents is used to form Mg-doped V_2O_5 (Figure S1A).[27] The x value in $Mg_xV_2O_5$ ranges from 0.05 to 0.15, as determined by the induction coupled plasma (ICP) method (Figure S1B). The XRD patterns (Figure S2) show that Mg-doped V_2O_5 remains as the layered α-phase, which is similar to undoped V_2O_5 but with a peak shift to higher d-spacing. This shift corresponds to Mg occupying interlayer sites within V_2O_5.[28] These sites are the same as those occupied by lithium during subsequent lithium intercalation.[29] High-resolution scanning transmission electron microscopy (HRTEM) results for V_2O_5 and $Mg_{0.10}V_2O_5$ (Figure S3A) show that both $Mg_{0.10}V_2O_5$ and pure V_2O_5 retain a layered phase, consistent with the XRD results. Energy-dispersive X-ray spectroscopy (EDS) mapping shows uniform distribution of Mg and V in the $Mg_{0.10}V_2O_5$ (Figure S3B). Finally, the chemical states of the V are characterized by X-ray photoelectron spectroscopy (XPS) in Figure S4. As Mg level increases, the average oxidation state of V decreases, as expected.

In the second step of forming Mg-doped LVO materials, Li is electrochemically intercalated into Mg-doped V_2O_5 to form the materials in situ. Figure 1A shows the voltage profiles during the lithiation step. Undoped V_2O_5 exhibits the regular $\alpha-\varepsilon-\delta$ phase transition when the Li intercalation amount (x in $Li_xV_2O_5$) ranges from 0 to 1.[30] Upon the introduction of Mg, the material shows a lower average potential during Li intercalation in the $\alpha-\delta$ region. The higher the Mg amount, the lower the potential. This is due to the initial oxidation state of V decreasing from V^{5+} with the cooperation of Mg (Figure S4). Furthermore, the transition to the $\delta-\gamma$ plateau takes place at a lower Li concentration, as Mg ions preoccupy the Li sites within the structure.[29] Starting from the $\delta-\gamma$ plateau, the potential profiles for different Mg doping levels become similar. Upon further Li intercalation, all materials reach the rocksalt ω phase, at a potential of ~1.5 V. The compositions of the materials obtained after the discharge were analyzed by ICP (Figure S5A), which confirmed the nominal compositions of the four materials: $Mg_{0.00}Li_3V_2O_5$, $Mg_{0.05}Li_{2.9}V_2O_5$, $Mg_{0.10}Li_{2.8}V_2O_5$, and $Mg_{0.15}Li_{2.7}V_2O_5$. These materials will be referred to as Mg0.00, Mg0.05, Mg0.10, and Mg0.15 hereafter.

Ex-situ synchrotron XRD (SXRD) and pair distribution function (PDF) data were utilized to examine the crystal structures. The SXRD patterns (Figure 1B) confirm that all materials form a DRS structure within the $Fn\bar{3}m$ space group. The supercell model of $Li_3V_2O_5$ shows good agreement with the PDF data for all degrees of Mg doping (Figure 2C, Figure S6), validating the DRS model on the local order. The distinct peak in the residual of the PDF refinement at ~5 Å can be assigned to local cation ordering.[31] Rietveld refinement results (Figure S7A-D) verify the DRS phase's presence with the

https://doi.org/10.1021/acsmaterialslett.4c02086
ACS Materials Lett. 2025, 7, 699−706

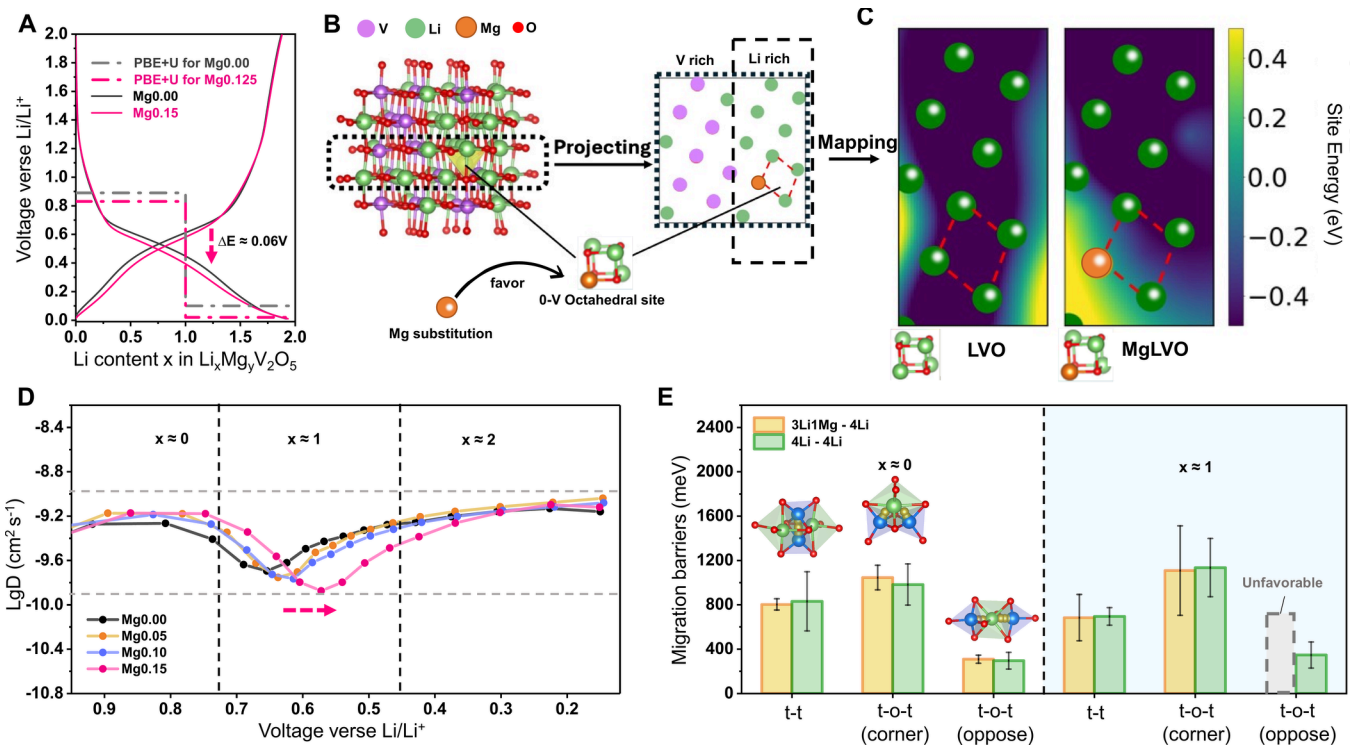

Figure 2. Observations and explanations of thermodynamics and kinetics. (A) Comparison of experimental (Mg0.00 and Mg0.15) and computational (Mg0.00 and Mg0.125) voltage profiles calculated from the PBE+U functional. (B) Schematic of Mg substitution in the Li-rich area. (C) Corresponding projection of site energy mapping of the supercell. (D) Comparison of diffusion coefficients calculated from GITT measurements. (E) Comparison of NEB barriers for possible Li migration hops between 4Li and 3Li1Mg sites. The error bars represent the standard deviation of the barriers.

lattice parameters for the four materials listed in Table S1. The average value of 4.096 Å is consistent with previous reports.[12] A slight expansion in *d*-spacing is observed in the Mg-doped materials.

HRTEM images of both Mg0.00 and Mg0.10 (Figures 1D and 1E) demonstrate good crystallinity consistent with the $Fn\bar{3}m$ space group. Fast Fourier transform (FFT) analysis reveals the (200) and (220) peaks are consistent with the cubic rock-salt structure and the Rietveld refinement findings. Energy-dispersive X-ray spectroscopy (EDS) mapping of the Mg-doped materials, depicted in Figure 1F, indicates uniform Mg doping across the sample. Notably, there is no excessive Mg accumulation at the particle edges, and the intensity of the Mg signal closely matches the EDS spectra in Figure S5B, suggesting a uniform Mg distribution within the bulk structure.

XPS results (Figure 1G) confirm the presence of Mg and reveal an increasing trend of Mg 2p intensity (relative to Li 1s) across the four materials, consistent with the ICP results. The valency of V plays a crucial role in the charge compensation mechanism.[12,32,33] The XPS spectra for V 2p (Figure S5C) indicate the exclusive presence of V^{4+} and V^{3+} ions in all materials, with peaks located at 516 and 515 eV, respectively. This results in an average valency of ∼3.5+ for V. Moreover, increasing Mg doping does not significantly alter the average valency of V. This observation is consistent with the expected charge balance in the nominal compositions discussed. These results have collectively validated the successful synthesis of Mg-doped LVO with a DRS structure.

To evaluate the performance of Mg-doped LVO as a potential anode material, Mg-doped V_2O_5 is fully lithiated by discharging to 0.01 V with voltage profiles shown in Figure S8. SXRD patterns (Figure S9A) demonstrate the retention of the DRS phase after full lithiation. Corresponding Rietveld refinement results (Figure S9B) indicate an increase in the *d*-spacing across all materials. The lattice parameters of fully lithiated materials are summarized in Table S1. The fully lithiated materials show an average volume expansion of ∼5.7% versus Mg-doped LVO materials formed at 1.5 V shown in Figure 1A, with a corresponding linear change of 1.9%. This is consistent with previous studies.[9] Mg-doped materials thus exhibit limited volume change, like the undoped material, underscoring their potential to be highly stable during cycling.

Figure 2A presents a comparison of the potential profiles for Mg-doped and undoped systems between 0.01 and 2.0 V obtained both experimentally and computationally. The experimental potential profile is acquired at a low rate of 0.02 A g^{-1} to approximate a thermodynamic measurement. Mg0.15 exhibits a noticeable downward shift in both the charge and discharge voltage profiles, with an average reduction of 0.06 V (∼10%). Voltage profiles for materials with varying Mg doping levels (Figure S10A) and corresponding differential capacity (dQ/dV) vs voltage plots (Figure S10B), consistently show a decrease in the voltage plateau as the Mg concentration increases. However, the capacities across all materials vary only slightly.

We next use PBE+U functional computation to understand the lower working potential of Mg-LVO. Due to computational constraints, it was not feasible to construct supercells with Mg0.10 or Mg0.15 as these would require significantly larger supercells. However, the Mg0.125 supercell provides a valuable approximation for understanding the effect of Mg doping. The observed changes of Li intercalation/extraction voltage (V),

https://doi.org/10.1021/acsmaterialslett.4c02086
ACS Materials Lett. 2025, 7, 699−706

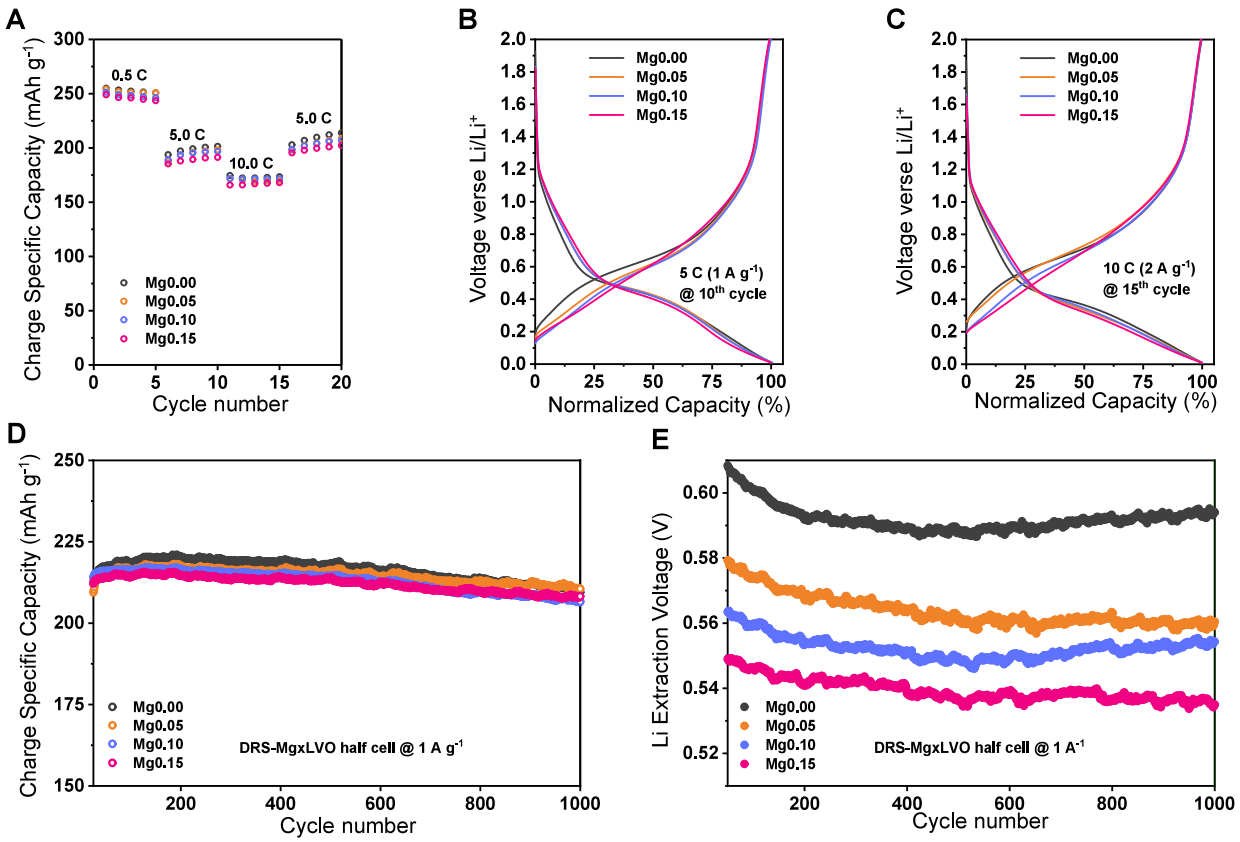

Figure 3. Half-cell performance evaluation of Mg-doped LVO. (A) Rate capability evaluation. Following the 10 C rate test, materials were cycled at 5 C (1 A g^{-1}) to evaluate long-term cycling stability. (B, C) Early cycle voltage profiles at 5 and 10 C. (D) Long-term cycling stability at 5 C (1 A g^{-1}) following the tests in panel (A). (E) Li extraction voltage for all materials over 1000 cycles.

$$V = \frac{E(\mathrm{Li}_{x_1}\mathrm{V_2O_5}) - E(\mathrm{Li}_{x_2}\mathrm{V_2O_5}) - (x_1 - x_2)E(\mathrm{Li})}{(x_1 - x_2)e} \quad (1)$$

are linked to the Li energy in the interstitial tetrahedral sites within the lattice (E represents the total DFT energy, e represents the electronic charge), as detailed in the Experimental Section. Equation 1 emphasizes the relationship between the site energy and voltage: during Li intercalation/extraction, a higher site energy results in a lower average potential. This direct correlation, which aligns with the level of difficulty of removing Li ions from the interstitial sites, underscores the impact of lattice site energies on the electrochemical performance of the anode material.

To directly observe the changes in site energy induced by Mg doping, Figure 2B illustrates a special quasi-random structure (SQS) of the DRS-LVO model superlattice consisting of eight formula units, with the projection of a layer of the superlattice containing the doped site. Details are listed in Table S2. As depicted in Figure 2C, the calculated Li site energies are subsequently mapped onto the projected layer before and after Mg substitution (at the Li-rich area only for clarity; the V-rich area in general has positive site energies which are unfavorable for Li intercalation). The Mg dopant prefers to substitute into the Li-rich area, thus transforming 4Li tetrahedral sites to 3Li1Mg sites (see the Experimental Section). As shown in Figure 2C, substituting Mg results in an increase in the site energy (weakening Li binding energy) for the nearby 3Li1Mg and 2Li1Mg interstitial sites. The incorporation of the Mg at an octahedral site in the Li-rich area reduces the level of difficulty of Li extraction at neighboring tetrahedral interstitial sites while maintaining a negative site energy. This results in the observed reduction of potential of 0.06 V from $x = 0$ to $x = 1$ in $\mathrm{Li}_{3+x-2y}\mathrm{Mg}_y\mathrm{V_2O_5}$, and a 0.08 V drop in the voltage from $x = 1$ to $x = 2$. Cumulatively, a total calculated average voltage reduction of 0.07 V from $x = 0$ to $x = 2$ by PBE+U functional aligns closely with the experimental observation of a 0.06 V drop (Figure 2A).

We next examine the kinetic effects of Mg doping. The diffusion coefficient was determined using the Galvanostatic Intermittent Titration Technique (GITT) method (Figure 2D). A comparison between Mg0.00 and Mg0.15 reveals that Mg doping slightly decreases the diffusivity of Li ions, indicating a modest reduction in kinetics. Despite this, a noticeable decrease in the delithiation potential, as shown in Figure 2A, is still observed, again confirming that the observed potential reduction is a thermodynamic effect. Overall, all materials exhibit similar Li diffusion coefficients, varying by only a single order of magnitude, suggesting comparable rate capabilities when used as electrode materials.

The impact of Mg doping on Li diffusion was further substantiated through computational analysis. Figure 2E presents the calculated Nudged Elastic Band (NEB) barriers for Li migration pathways (t-o-t (corner), t-o-t (oppose), t-t, where t represents tetrahedral site and O represents octahedral site) in two different site configurations: from 4Li-to-4Li sites and from 4Li-to-3Li1Mg sites (for sites configuration, please refer to Figure S11). Additionally, two distinct regions with different lithium intercalation amounts ($x \approx 0$ and 1) are compared (Figures S12 and S13). No significant differences are observed in the migration barriers for Li hopping between

https://doi.org/10.1021/acsmaterialslett.4c02086
ACS Materials Lett. 2025, 7, 699−706

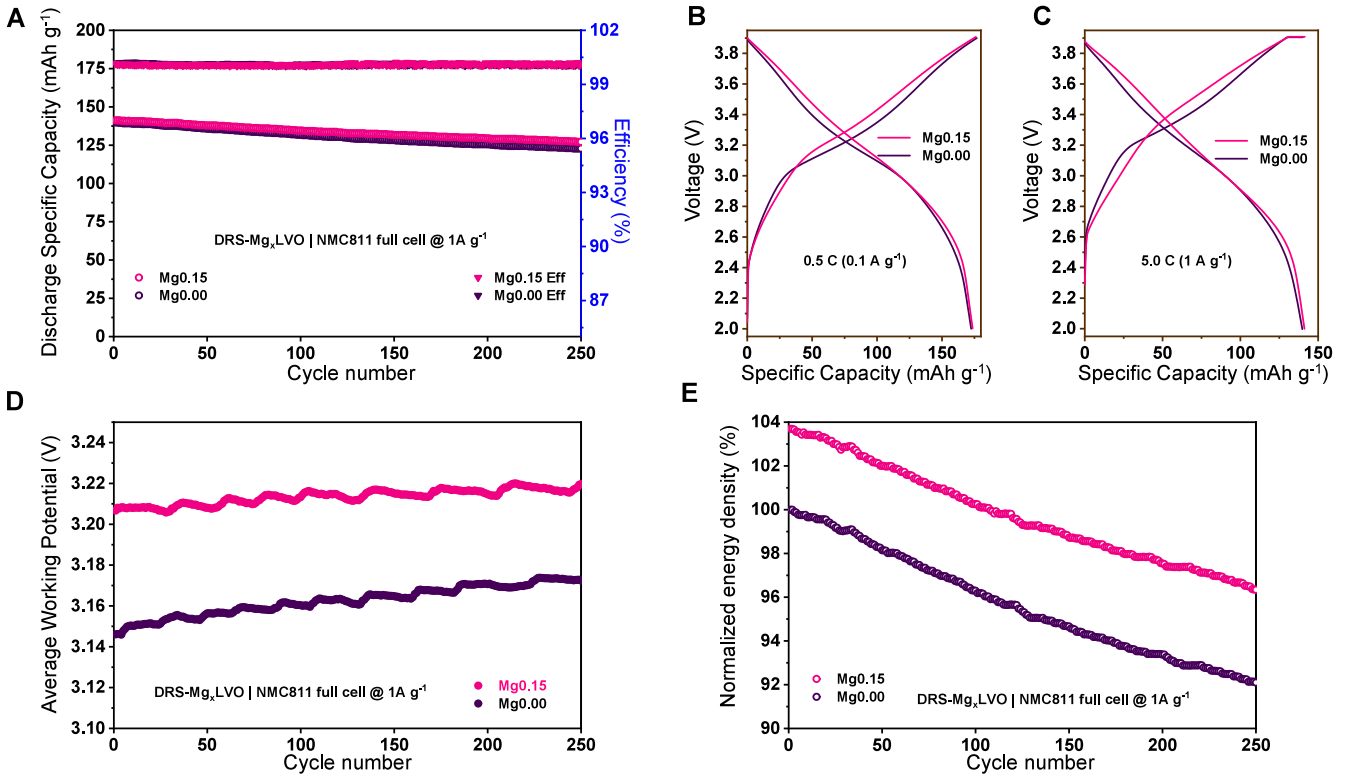

Figure 4. Full cell performance using Mg-doped LVO anodes. (A) Cycling stability of DRS-Mg$_x$LVO | NMC811 full cell at 1 A g^{-1}. (B, C) Comparison of full cell voltage profiles at 0.1 A g^{-1} and 1 A g^{-1}. (D, E) Comparison of full-cell average working voltage and gravimetric energy density over 250 cycles. (Gravimetric energy density is normalized to Mg0.00.)

tetrahedrons (t-t) and corner-shared octahedrons (t-o-t corner) in either region. An increase in the migration barriers is found for pathways opposing empty shared octahedrons (t-o-t oppose) in the presence of Mg. This indicates a strong repulsive force from Mg toward migrating Li, thereby making the t-o-t oppose migration pathway less favorable. This computational result correlates with the experimental finding that Mg-doped materials demonstrate a marginally reduced diffusion coefficient in the region where ∼1 Li is intercalated. The implications of these kinetic observations on the uncompromised rate performance will be further discussed in the context of half-cell tests.

Half-cell tests of the four materials against Li-metal counter-electrodes are first used to evaluate their rate capabilities (Figure 3A). Here, the C rate is defined assuming a capacity of 200 mAh g^{-1} between 0.01 and 2.0 V. All four materials exhibit excellent and similar rate capabilities, indicating that Mg doping has a negligible impact on the kinetics. The voltage profiles obtained under high-rate tests (5 and 10 C) are shown in Figures 3B and 3C. To facilitate the comparison, the capacities are normalized. A downward shift in voltage is observed, with the Li extraction voltage (average voltage between 0.01 and 2 V) listed in Table S3. Mg0.15 exhibits the largest voltage difference, ∼0.06 V at 5 C and ∼0.07 V at 10 C. These results are also consistent with the trends seen at low rates (Figure S10). Moreover, Figures S14A and S14B show the voltage profiles at different rates for Mg0.00 and Mg0.15. Mg0.15 has comparable rate capability to Mg0.00 but exhibits lower charge potential at all rates.

Figure 3D presents the capacity retention tested at a 5 C rate over 1000 cycles, showing that all materials maintain over 95% of their capacity throughout cycling. The minor capacity decay observed near the 1000th cycle can be attributed to the degradation of the Li metal counter electrode under high-rate cycling conditions.[12] Figure 3E compares the Li extraction voltage of the four materials, showing that a voltage difference persists throughout cycling, with Mg0.15 maintaining a potential of 0.54 V vs Li. Figure S15 compares the voltage profiles of the four materials at the 1000th cycle, revealing that an ∼0.06 V voltage difference persists between Mg0.00 and Mg0.15. Finally, electrode characterization for Mg0.00 and Mg0.15, shown in Figures S16 and S17, confirms the absence of obvious cracks after cycling. Furthermore, cross-sectional SEM images in Figure S18 reveal no significant thickness changes in the electrodes, further supporting the minimal volume change of the DRS materials. These results highlight the materials' robust structural stability, consistent with findings from structural analyses.

To demonstrate the practical application of the Mg-doped materials with suppressed potential, we paired Mg0.00 and Mg0.15 with a $LiNi_{0.8}Mn_{0.1}Co_{0.1}O_2$ (NMC811) cathode at a negative/positive electrode capacity ratio of 1.1:1. Figure 4A shows the cycling stability at a rate of 1 A g^{-1} in the range of 2 to 3.9 V. Both full cells exhibit a good rate capability of ∼140 mAh $g_{cathode}^{-1}$ with minimal capacity variation. The slight capacity fade observed in both cells during cycling can be attributed to degradation of the NMC cathodes under high-rate cycling conditions.[12] The voltage profiles (Figures 4B and 4C) obtained at 0.1 A g^{-1} and 1 A g^{-1} show a noticeable higher voltage for the cell with the Mg0.15 anode, confirming the translation of half-cell voltage improvements to full-cell behavior. In addition, the energy efficiencies of both cells (Table S4) are close to 90%, with Mg0.15 slightly higher than Mg0.00.

https://doi.org/10.1021/acsmaterialslett.4c02086
ACS Materials Lett. 2025, 7, 699−706

Figure 4D presents the average working potential of both cells throughout the cycles. Mg0.15 exhibited an average voltage of 3.21 V, around 0.06 V higher than Mg0.00. This improvement persists over 250 cycles. There is a slight increase in the working potential with cycling, particularly for the full cell with the undoped LVO anode. This is consistent with the decrease in the working potential during the initial cycles observed in the half-cell test (Figure 3D). We posit that this is related to stabilization of the DRS structure after being transformed from the original layered structure under high-rate cycling conditions. Finally, as a result of the higher working potential, the gravimetric energy density of the cell with Mg0.15 is ∼4% higher than Mg0.00.

In conclusion, we explored the effects of Mg doping on the DRS anode material, LVO, analyzing its impact on both thermodynamics and kinetics through a combination of experimental investigations and DFT calculations. The introduction of Mg ions at octahedral sites increases the site energy of nearby Li ions, reducing their binding energy and thus facilitating Li extraction from adjacent tetrahedral sites. This mechanism contributes to a ∼ 10% reduction in the potential plateau by ∼0.06 V for the Mg0.15, relative to the Mg0.00. As a result, this material achieves a working potential of 0.54 V, the lowest reported among fast-charging oxide anode materials. From a kinetic standpoint, the influence of Mg doping on Li migration has been found to be minimal. Half-cell experiments demonstrate that Mg doping preserves the advantages of undoped LVO, Mg0.00, specifically its excellent rate capability and cycling stability, while offering the benefit of reducing the working potential. Full-cell assessments show a ∼0.06 V increase in working potential for Mg0.15 compared to Mg0.00 when cycled at 1 A g^{-1}. This voltage improvement, along with a comparable capacity, translates into an enhancement of the energy density by ∼4%. Future research will explore other doping elements and optimized doping concentrations to further enhance energy density and cycling stability. Our findings point to the potential of DRS anode material to enable long-life batteries for V2G applications.

■ ASSOCIATED CONTENT

Data Availability Statement

The data that support the findings of this study are available from the corresponding author upon reasonable request.

Supporting Information

The Supporting Information is available free of charge at https://pubs.acs.org/doi/10.1021/acsmaterialslett.4c02086.

Experimental details, computational details, synthesis, additional material characterizations (ICP, XPS, SEM, TEM), additional electrochemical studies (PDF)

■ AUTHOR INFORMATION

Corresponding Authors

Ping Liu − *Aiiso Yufeng Li Family Department of Nanoengineering and Sustainable Power and Energy Center, University of California San Diego, La Jolla, California 92093, United States;* orcid.org/0000-0002-1488-1668; Email: piliu@ucsd.edu

Shyue Ping Ong − *Aiiso Yufeng Li Family Department of Nanoengineering and Sustainable Power and Energy Center, University of California San Diego, La Jolla, California 92093, United States;* orcid.org/0000-0001-5726-2587; Email: ongsp@ucsd.edu

Karena W. Chapman − *Department of Chemistry, Stony Brook University, Stony Brook, New York 11794, United States;* orcid.org/0000-0002-8725-5633; Email: karena.chapman@stonybrook.edu

Authors

Haichen Lin − *Aiiso Yufeng Li Family Department of Nanoengineering and Sustainable Power and Energy Center, University of California San Diego, La Jolla, California 92093, United States*

Wei-Tao Peng − *Sustainable Power and Energy Center, University of California San Diego, La Jolla, California 92093, United States;* Present Address: Department of Chemistry, Tunghai University, Taichung 407224, Taiwan

Zishen Wang − *Sustainable Power and Energy Center, University of California San Diego, La Jolla, California 92093, United States;* orcid.org/0000-0003-0578-2868

Jan Hofmann − *Department of Chemistry, Stony Brook University, Stony Brook, New York 11794, United States;* orcid.org/0000-0002-0182-9174

Simon M. Vornholt − *Department of Chemistry, Stony Brook University, Stony Brook, New York 11794, United States*

Haodong Liu − *Aiiso Yufeng Li Family Department of Nanoengineering and Sustainable Power and Energy Center, University of California San Diego, La Jolla, California 92093, United States*

Shen Wang − *Sustainable Power and Energy Center, University of California San Diego, La Jolla, California 92093, United States*

John Holoubek − *Aiiso Yufeng Li Family Department of Nanoengineering and Sustainable Power and Energy Center, University of California San Diego, La Jolla, California 92093, United States; Department of Chemistry, Stony Brook University, Stony Brook, New York 11794, United States*

Ke Zhou − *Sustainable Power and Energy Center, University of California San Diego, La Jolla, California 92093, United States*

Qiushi Miao − *Sustainable Power and Energy Center, University of California San Diego, La Jolla, California 92093, United States;* orcid.org/0009-0008-0857-6107

Steven Huber − *Aiiso Yufeng Li Family Department of Nanoengineering and Sustainable Power and Energy Center, University of California San Diego, La Jolla, California 92093, United States*

Complete contact information is available at: https://pubs.acs.org/10.1021/acsmaterialslett.4c02086

Author Contributions

CRediT: **Haichen Lin** conceptualization, data curation, formal analysis, investigation, methodology, validation, writing - original draft, writing - review & editing; **Wei-Tao Peng** conceptualization, data curation, formal analysis, investigation, methodology, validation, visualization, writing - original draft, writing - review & editing; **Zishen Wang** data curation, formal analysis, methodology, validation, writing - original draft, writing - review & editing; **Jan Hofmann** data curation, formal analysis, methodology, writing - review & editing; **Simon M. Vornholt** data curation, methodology; **Haodong Liu** conceptualization, writing - review & editing; **Shen Wang** data curation; **John Jaeun Holoubek** data curation, formal analysis; **Ke Zhou** writing - review & editing; **Qiushi Miao** data curation; **Steven Huber** writing - review & editing; **Karena W**

https://doi.org/10.1021/acsmaterialslett.4c02086
ACS Materials Lett. 2025, 7, 699−706

Chapman methodology, resources, supervision, writing - review & editing; **Shyue Ping Ong** conceptualization, methodology, resources, software, supervision, writing - review & editing; **Ping Liu** conceptualization, funding acquisition, methodology, project administration, resources, supervision, writing - review & editing.

Notes

The authors declare the following competing financial interest(s): A patent disclosure is filed with University of California San Diegos Office of Innovation and Commercialization.

■ ACKNOWLEDGMENTS

This work was partially supported as part of GENESIS: A Next Generation Synthesis Center, an Energy Frontier Research Center funded by the U.S. Department of Energy, Office of Science, Basic Energy Sciences under Award No. DE-SC0019212 to P.L and K.C. The computational portions of this work used Expanse at the San Diego Supercomputer Center. This work was performed in part at the San Diego Nanotechnology Infrastructure (SDNI) of UCSD, a member of the National Nanotechnology Coordinated Infra-structure (NNCI), which is supported by the National Science Foundation (Grant No. ECCS-1542148). This research used resources of the Advanced Photon Source, a U.S. Department of Energy (DOE) Office of Science User Facility operated for the DOE Office of Science by Argonne National Laboratory under Contract No. DE-AC02-06CH11357.

■ REFERENCES

(1) Liu, J.; Bao, Z.; Cui, Y.; Dufek, E. J.; Goodenough, J. B.; Khalifah, P.; Li, Q.; et al. Pathways for Practical High-Energy Long-Cycling Lithium Metal Batteries. *Nat. Energy* **2019**, *4*, 180−186.

(2) Xu, H.; Zhang, J.; Zhang, H.; Long, J.; Xu, L.; Mai, L. In Situ Topological Interphases Boosting Stable Solid-State Lithium Metal Batteries. *Adv. Energy Mater.* **2023**, *13*, 2204411.

(3) Zhang, N.; Du, L.; Zhang, J.; Xu, H.; Zhou, X.; Mai, L.; Xu, L. Self-Assembled Tent-Like Nanocavities for Space-Confined Stable Lithium Metal Anode. *Adv. Funct. Mater.* **2023**, *33*, 2210862.

(4) Liu, J.; Xiao, J.; Yang, J.; Wang, W.; Shao, Y.; Liu, P.; Whittingham, M. S. The TWh Challenge: Next Generation Batteries for Energy Storage and Electric Vehicles. *Next Energy* **2023**, *1*, 100015.

(5) Dik, A.; Omer, S.; Boukhanouf, R. Electric Vehicles: V2G for Rapid, Safe, and Green EV Penetration. *Energies* **2022**, *15*, 803.

(6) Yilmaz, M.; Krein, P. T. Review of the Impact of Vehicle-to-Grid Technologies on Distribution Systems and Utility Interfaces. *IEEE Trans. Power Electron.* **2013**, *28*, 5673−5689.

(7) Shi, Q.; Heng, S.; Qu, Q.; Gao, T.; Liu, W.; Hang, L.; Zheng, H. Constructing an Elastic Solid Electrolyte Interphase on Graphite: A Novel Strategy Suppressing Lithium Inventory Loss in Lithium-Ion Batteries. *J. Mater. Chem. A* **2017**, *5*, 10885−10894.

(8) Schweidler, S.; de Biasi, L.; Schiele, A.; Hartmann, P.; Brezesinski, T.; Janek, J. Volume Changes of Graphite Anodes Revisited: A Combined Operando X-ray Diffraction and In Situ Pressure Analysis Study. *J. Phys. Chem. C* **2018**, *122*, 8829−8835.

(9) Odziomek, M.; Chaput, F.; Rutkowska, A.; Świerczek, K.; Olszewska, D.; Sitarz, M.; Lerouge, F.; Parola, S. Hierarchically Structured Lithium Titanate for Ultrafast Charging in Long-Life High-Capacity Batteries. *Nat. Commun.* **2017**, *8*, 15636.

(10) Shen, L.; Chen, S.; Maier, J.; Yu, Y. Carbon-Coated Li_3VO_4 Spheres as Constituents of an Advanced Anode Material for High-Rate Long-Life Lithium-Ion Batteries. *Adv. Mater.* **2017**, *29*, 1701571.

(11) Inada, R.; Mori, T.; Kumasaka, R.; Ito, R.; Tojo, T.; Sakurai, Y. Characterization of Vacuum-Annealed $TiNb_2O_7$ as a High-Potential Anode Material for Lithium-Ion Batteries. *Int. J. Appl. Ceram. Technol.* **2019**, *16*, 264−272.

(12) Liu, H.; Zhu, Z.; Yan, Q.; Yu, S.; He, X.; Chen, Y.; Zhang, R.; Ma, L.; Liu, T.; Li, M.; et al. A Disordered Rock Salt Anode for Fast-Charging Lithium-Ion Batteries. *Nature* **2020**, *585*, 63−67.

(13) Hu, B.; Wang, X.; Xu, J.; Ding, J.; Ge, S. Chemically Synthesized Nano-$Li_3V_2O_5$ Anode for High-Rate Rechargeable Li-Ion Batteries at Low Temperature. *J. Energy Storage* **2023**, *66*, 107472.

(14) Lan, X.; Wang, L.; Yu, L.; Li, Y.; Hu, X. Synergy of Highly Reversible ω-$Li_3V_2O_5$ Anodes and Fluorine-Containing Additive Electrolytes Promises Low-Temperature-Tolerant Li-Ion Batteries. *ACS Mater. Lett.* **2021**, *3*, 1394−1401.

(15) Wang, Z.; Yuan, S.; Tang, X.; Wang, H.; Zhang, M.; Liu, F.; Yao, N.; Ma, Y. Enhanced Li-Ion Migration Behavior in $Li_3V_2O_5$ Rock-Salt Anode via Stepwise Lattice Tailoring. *Energy Storage Mater.* **2023**, *54*, 284−293.

(16) Kuznetsov, D. A.; Han, B.; Yu, Y.; Rao, R. R.; Hwang, J.; Román-Leshkov, Y.; Shao-Horn, Y. Tuning Redox Transitions via Inductive Effect in Metal Oxides and Complexes, and Implications in Oxygen Electrocatalysis. *Joule* **2018**, *2*, 225−244.

(17) Li, H.; Fong, R.; Woo, M.; Ahmed, H.; Seo, D.-H.; Malik, R.; Lee, J. Toward High-Energy Mn-Based Disordered-Rocksalt Li-Ion Cathodes. *Joule* **2022**, *6*, 53−91.

(18) Li, H.; Zhou, P.; Liu, F.; Li, H.; Cheng, F.; Chen, J. Stabilizing Nickel-Rich Layered Oxide Cathodes by Magnesium Doping for Rechargeable Lithium-Ion Batteries. *Chem. Sci.* **2019**, *10*, 1374−1379.

(19) Hwang, D.-Y.; Kim, H.-S.; Lee, S.-H. Highly Stable and High-Performance $MgHPO_4$ Surface-Modified Ni-Rich Cathode Materials for Advanced Lithium-Ion Batteries. *J. Mater. Chem. A* **2022**, *10*, 16555−16569.

(20) Kong, F.; Longo, R. C.; Yeon, D.-H.; Yoon, J.; Park, J.-H.; Liang, C.; KC, S.; Zheng, Y.; Doo, S.-G.; Cho, K. Multivalent Li-Site Doping of Mn Oxides for Li-Ion Batteries. *J. Phys. Chem. C* **2015**, *119*, 21904−21912.

(21) Li, H.; Zhao, X.; Li, Y.; Gan, Y.; Qiu, W.; Wang, J.; Liu, J. Alkaline-Earth Metal Substitution Stabilizes the Anionic Redox of Li-Rich Oxides. *J. Mater. Chem. A* **2021**, *9*, 10364−10373.

(22) Levi, E.; Levi, M. D.; Chasid, O.; Aurbach, D. A Review on the Problems of Solid-State Ion Diffusion in Cathodes for Rechargeable Mg Batteries. *J. Electroceram.* **2009**, *22*, 13−19.

(23) Sallard, S.; Sheptyakov, D.; Villevieille, C. Improved Electrochemical Performances of Li-Rich Nickel Cobalt Manganese Oxide by Partial Substitution of Li^+ by Mg^{2+}. *J. Power Sources* **2017**, *359*, 27−36.

(24) Liu, Y.; Chang, C.; Zheng, J. Revealing the Role of Mg Doping in $LiFe_{0.39}Mg_{0.01}Mn_{0.6}PO_4$/C Cathode: Enhanced Electrochemical Performance from Improved Electrical Conductivity and Promoted Lithium Diffusion Kinetics. *J. Energy Storage* **2024**, *91*, 112108.

(25) Torres-Castro, L.; Abreu-Sepulveda, M. A.; Katiyar, R. S.; Manivannan, A. Electrochemical Investigations on the Effect of Mg-Substitution in Li_2MnO_3 Cathode. *J. Electrochem. Soc.* **2017**, *164*, A1464.

(26) Zhong, P.; Cai, Z.; Zhang, Y.; Giovine, R.; Ouyang, B.; Zeng, G.; Chen, Y.; Clément, R.; Lun, Z.; Ceder, G. Increasing Capacity in Disordered Rocksalt Cathodes by Mg Doping. *Chem. Mater.* **2020**, *32*, 10728−10736.

(27) Koketsu, T.; Ma, J.; Morgan, B. J.; Body, M.; Legein, C.; Dachraoui, W.; Giannini, M.; et al. Reversible Magnesium and Aluminium Ions Insertion in Cation-Deficient Anatase TiO_2. *Nat. Mater.* **2017**, *16*, 1142−1148.

(28) Fu, Q.; Sarapulova, A.; Trouillet, V.; Zhu, L.; Fauth, F.; Mangold, S.; Welter, E.; et al. *In Operando* Synchrotron Diffraction and *In Operando* X-ray Absorption Spectroscopy Investigations of Orthorhombic V_2O_5 Nanowires as Cathode Materials for Mg-Ion Batteries. *J. Am. Chem. Soc.* **2019**, *141*, 2305−2315.

(29) Mukherjee, A.; Sa, N.; Phillips, P. J.; Burrell, A.; Vaughey, J.; Klie, R. F. Direct Investigation of Mg Intercalation into the Orthorhombic V_2O_5 Cathode Using Atomic-Resolution Transmission Electron Microscopy. *Chem. Mater.* **2017**, *29*, 2218−2226.

https://doi.org/10.1021/acsmaterialslett.4c02086
ACS Materials Lett. 2025, 7, 699−706

(30) Delmas, C.; Cognac-Auradou, H.; Cocciantelli, J. M.; Ménétrier, M.; Doumerc, J. P. The $Li_xV_2O_5$ System: An Overview of the Structure Modifications Induced by the Lithium Intercalation. *Solid State Ionics* **1994**, *69*, 257−264.
(31) Wang, Y.; Huang, S.; Raji-Adefila, B.; Outka, A.; Wang, J.-H.; Chen, D. Unraveling the Nature and Role of Layered Cation Ordering in Cation-Disordered Rock-Salt Cathodes. *J. Am. Chem. Soc.* **2022**, *144*, 19838−19848.
(32) Kallquist, I.; Naylor, A. J.; Baur, C.; Chable, J.; Kullgren, J.; Fichtner, M.; Edstrom, K.; Brandell, D.; Hahlin, M. Degradation Mechanisms in Li_2VO_2F Li-Rich Disordered Rock-Salt Cathodes. *Chem. Mater.* **2019**, *31*, 6084−6096.
(33) Babar, M.; Hafiz, H.; Ahmad, Z.; Barbiellini, B.; Bansil, A.; Viswanathan, V. Effect of Disorder and Doping on Electronic Structure and Diffusion Properties of $Li_3V_2O_5$. *J. Phys. Chem. C* **2022**, *126*, 15549−15557.

https://doi.org/10.1021/acsmaterialslett.4c02086
ACS Materials Lett. 2025, 7, 699−706